



HAL
open science

Experimental full wavefield reconstruction and band diagram analysis in a single-phase phononic plate with internal resonators

N. Kherraz, M. Radziński, M. Mazzotti, P. Kudela, F. Bosia, A. S. Gliozzi, D. Misseroni, N. M. Pugno, W. Ostachowicz, M. Miniaci

► **To cite this version:**

N. Kherraz, M. Radziński, M. Mazzotti, P. Kudela, F. Bosia, et al.. Experimental full wavefield reconstruction and band diagram analysis in a single-phase phononic plate with internal resonators. *Journal of Sound and Vibration*, 2021, 503, pp.116098. <10.1016/j.jsv.2021.116098>. <hal-03440709>

HAL Id: hal-03440709

<https://hal.science/hal-03440709v1>

Submitted on 22 Nov 2021

HAL is a multi-disciplinary open access archive for the deposit and dissemination of scientific research documents, whether they are published or not. The documents may come from teaching and research institutions in France or abroad, or from public or private research centers.

L'archive ouverte pluridisciplinaire **HAL**, est destinée au dépôt et à la diffusion de documents scientifiques de niveau recherche, publiés ou non, émanant des établissements d'enseignement et de recherche français ou étrangers, des laboratoires publics ou privés.



HAL Authorization

Experimental full wavefield reconstruction and band diagram analysis in a single-phase phononic plate with internal resonators

N. Kherraz^a, M. Radziński^b, M. Mazzotti^c, P. Kudela^b, F. Bosia^d, A. S. Gliozzi^d, D. Misseroni^e, N.M. Pugno^{e,f}, W. Ostachowicz^b, M. Miniaci^{a,*}

a) CNRS, Univ. Lille, Ecole Centrale, ISEN, Univ. Valenciennes, IEMN - UMR 8520, 59046, Lille cedex, France

b) Institute of Fluid-Flow Machinery, Polish Academy of Science, Fiszerka 14 st. 80-231 Gdańsk, Poland

c) Department of Mechanical Engineering, CU Boulder, 1111 Engineering Drive, UCB 427 Boulder, CO 80309, USA

d) Department of Applied Science and Technology, Politecnico di Torino, Corso Duca degli Abruzzi 24, 10124, Torino, Italy

e) Laboratory of Bio-Inspired, Bionic, Nano, Meta Materials & Mechanics, Department of Civil, Environmental and Mechanical Engineering, University of Trento, Via Mesiano77, 38123 Trento, Italy

f) Queen Mary University of London, School of Engineering, Materials Science, Mile End Road, London E1 4NS, UK

Abstract

Research on phononic crystal architectures has produced many interesting designs in the past years, with useful wave manipulation properties. However, not all of the proposed designs can lead to convenient realizations for practical applications, and only a limited number of them have actually been tested experimentally to verify numerical estimations and demonstrate their feasibility.

In this work, we propose a combined numerical-experimental procedure to characterize the dynamic behavior of metamaterials, starting from a simplified 2D design to a real 3D manufacturing structure. To do this, we consider a new simplified design of a resonator-type geometry for a phononic crystal, and verify its wave filtering properties in wave propagation experiments. The proposed geometry exploits a circular distribution of cavities in a homogeneous material, leading to a central resonator surrounded by thin ligaments and an external matrix. Parametric simulations are performed to determine the optimal thickness of this design leading to a large full band gap in the kHz range. Full field experimental characterization of the resulting phononic crystal using a scanning laser Doppler vibrometer is then performed, showing excellent agreement with numerically predicted band gap prop-

*correspondence to: Marco Miniaci, tel +39 329 22 59 031, email: marco.miniaci@univ-lille.fr
Preprint submitted to Elsevier

32 erties and with their resulting effects on propagating waves. The outlined procedure can
33 serve as a useful step towards a standardization of metamaterial development and validation
34 procedures.

35 *Keywords: Phononic Crystals, Elastic Metamaterials, Elastic Wave Propagation,*
36 *Experimental Full Wavefield Reconstruction, Wavenumber-Frequency Analysis*

37 1. Introduction

38 The investigation of elastic wave propagation phenomena in artificially structured com-
39 posite materials is an active research topic in the scientific community. Shortly after the
40 introduction of photonic crystals and electromagnetic metamaterials, their elastic counter-
41 part, i.e., phononic crystals (PCs) and elastic metamaterials [1–3], have attracted increasing
42 attention due to the possibility of reproducing in elasticity an abundant set of unusual phys-
43 ical properties [4], such as stop-band filtering [5, 6], negative refraction [7–9], acoustic lens-
44 ing [10], ordinary [11, 12] and topologically protected [13–17] wave localization / splitting,
45 and fluid elasticity [18]. Among these, the ability to attenuate elastic waves over entire fre-
46 quency ranges, often referred to as phononic band gaps (BGs), is among the most attractive
47 and studied properties. BGs occur due to three main mechanism: Bragg scattering, local
48 resonance and inertial amplification [19–27].

49 Due to this property, phononic plates received great attention because of their potential
50 for technological applications: structural health monitoring [28, 29], wave switching [30] and
51 demultiplexing [31], micro-electro-mechanical systems [32, 32], cloaking [33], to cite a few.
52 Among the possible configurations, phononic plates made of single or multiple constituents
53 have been considered, including periodic distributions of inclusions, pillars / gratings on the
54 plate surfaces, and empty holes [34].

55 In multi-material phononic plates, the shape, material type as well as the orientation of
56 the inclusions strongly influence the existence and location in frequency of the BGs. The
57 possibility to open both Bragg and locally resonant BG types was reported [35–37]. In single
58 phase phononic crystals, it was shown that the local resonance of the pillars / inclusions was
59 the dominant mechanism to open / shift BGs [38, 39]. Plates with a periodic grating on the
60 surface have also been investigated, and a relationship established between the width of the

61 BG and the depth of the grooves [40]. While these two approaches inevitably lead to some
62 geometrical / manufacturing complexity, phononic plates realized by through-the-thickness
63 cavities in a homogeneous material remain a good compromise between a simpler fabrication
64 procedure and good wave attenuation performance. Whilst numerical / theoretical works
65 dealing with cavities perpendicular to the wave propagation plane are numerous, experimen-
66 tal measurements are often limited to few measurement points or small scanning regions. Our
67 aim in this paper is thus to propose an in-depth numerical and experimental characterization
68 procedure to validate metamaterial designs and develop them into functioning realistic struc-
69 tures. Inspired by the 2D geometry proposed for the first time by Bigoni and coworkers [10],
70 here, we first investigate the influence of extending the design into a 3D realistic single-phase
71 phononic plate with internal resonators generated by symmetrically arranged cavities, and
72 then provide experimental evidence of a complete BG in the kHz frequency range. Full wave-
73 field reconstruction of the wave propagation phenomena and a band diagram analysis in the
74 wavenumber-frequency domain is provided and compared to numerical calculations.

75 **2. Design of the phononic plate**

76 *2.1. Eigenvalue problem*

77 In this section, we numerically investigate the dispersion properties of a periodic structure
78 consisting of an inertial resonator embedded in a matrix through 8 ligaments, as shown in
79 Fig. 1A. The structure is obtained by milling 8 cavities arranged in an octagonal pattern in
80 a homogeneous Polymethyl methacrylate (PMMA, Perspex Black from Bayer) block, which
81 divides the cell into three regions, named matrix, ligaments and resonator, respectively. This
82 arrangement of material and cavities represents a good alternative to multi-phase resonators
83 often made of a heavy core (in steel, tungsten or similar heavy metals) surrounded by a soft
84 core (rubber, for instance) and embedded in an external matrix (often a polymer) [3]. In our
85 case, the ligaments play the role of the soft coating.

86 In-plane geometrical parameters of the unit cell are given as a function of the ligament
87 thickness $t = 1$ mm as follows: $A = 19 \cdot t = 19$ mm, $R_e = 9 \cdot t$, $R_i = 4 \cdot t$, as illustrated in
88 Fig. 1A. These parameters have been chosen with specimen fabrication in mind (i.e., with
89 the technical limitations of the milling process in mind). The density of PMMA is $\rho = 1180$

90 kg/m³ and the longitudinal and shear wave velocities are $c_L = 2665$ m/s and $c_T = 1363$ m/s,
 91 respectively.

92 As a first step, the band structures are computed considering an infinitely duplicated unit
 93 cell in a periodic square array, and considering elastic wave propagation in the linear elastic
 94 regime (under the hypothesis of small displacements). The unit cell domain is meshed by
 95 means of 8-node hexagonal elements of maximum size $L_{FE} = 0.1$ mm, which is found to
 96 provide accurate eigensolutions up to the frequency of interest [41]. Therefore, the resulting
 97 eigenvalue problem $(\mathbf{K} - \omega^2\mathbf{M})\mathbf{u} = \mathbf{0}$ is solved by varying the non-dimensional wavevector
 98 \mathbf{k}^* along the irreducible path $[M - \Gamma - X - M]$, with $M \equiv (\pi/A, \pi/A)$, $\Gamma \equiv (0, 0)$ and
 99 $X \equiv (\pi/A, 0)$ (see Fig. 1B), being A the lattice parameter, namely the unit cell side.

100 The corresponding band diagrams are presented in Fig. 2A for different height to the
 101 lattice parameter ratios $H/A = [0.1, 0.5, 0.8, 1.0, 1.2]$. The dispersion curves are color coded
 102 according to the height H of the unit cell. Specifically, the color bar of Fig. 2A varies
 103 gradually from dark blue (very thin unit cells) to dark red (thicker ones). The influence
 104 of the unit cell height on the dispersion curves is clearly visible from the diagrams. When
 105 an extremely flexible unit cell in the out-of-plane direction is considered (very small H/A
 106 ratio, for instance 0.1), no complete BG is visible in the diagram. This is due to a very low
 107 stiffness of the unit cell with respect to out-of-plane deformations, implying a large number
 108 of dispersion branches in the $[0 - 70]$ kHz frequency range. When the height to the lattice
 109 parameter ratio H/A increases, the structure gains stiffness against out-of-plane deformations
 110 and some of the previous modes migrate to higher frequencies. As a consequence, fewer curves
 111 are visible in the diagram in the same frequency range (compare for instance $H/A = 0.1$ to
 112 $H/A = 0.5$). In addition, specific modes (reported in Fig. 2B,C and highlighted in Fig. 2A by
 113 black arrows), undergo an opposite shift to higher / lower frequencies. This allows to open a
 114 BG of up to 8 kHz, achieved when $H/A = 1$, and ranging approximately from 45 to 53 kHz.
 115 *To gain a full understandings of the governing mechanism of the BG opening, we computed*
 116 *the imaginary part of the wavenumber, $\Im k(\omega)$, in the vicinity of the BG frequencies. The*
 117 *so-called $k(\omega)$ method has been adopted [42]. Figure 3A presents the imaginary part of the*
 118 *wavenumber, $\Im k(\omega)$, of the dispersion curves along the $\Gamma - X$ path for the $H/A = 1$ case, in*
 119 *the 40 – 60 kHz frequency range. Examining the curves exhibiting the lowest values of $\Im k(\omega)$*

120 *in proximity of the BG frequency (those indicated by the black arrows), it is possible to notice*
121 *the presence of both a parabolic and a spike-like behavior (Fig. 3B), both contributing to the*
122 *BG opening. This clearly proves that the considered structure opens a hybrid BG based on the*
123 *interaction of both Bragg and local resonance mechanisms. If the ratio H/A increases above*
124 *unity, additional bands are introduced again in the $[0 - 70]$ kHz frequency range reducing*
125 *the BG width (see for instance the flexural mode reported in Fig. 2D).*

126 *2.2. Numerical and experimental time-transient analysis on the finite structure*

127 In this section, a numerical time transient analysis on a finite structure is performed, and
128 compared to experimental measurements, as schematically indicated in Fig. 4. In view of the
129 experimental phase, a PMMA rectangular plate of length $4 \cdot L1 = 1000$ mm, width $2 \cdot L1 = 500$
130 mm and height $H = A = 19$ mm is considered. PMMA has been chosen as the material
131 composing both the matrix and the inertial resonators because of wide availability and the
132 possibility of manufacturing it with standard tools such as a milling machine. A PC region
133 made of 200 unit cells such as the one reported in Fig. 1A disposed in the shape of square
134 rings is introduced on the right side of the plate, as shown in Fig. 4A. In particular, the unit
135 cells are distributed over a square frame of external and internal widths of $15A$ and $5A$. An
136 unaltered area of $5A \times 5A = 95 \times 95$ mm² is therefore included in the center of the phononic
137 region. The sample used for the experimental analysis is manufactured by exporting the
138 geometry from the finite element model, and importing it to the milling machine (EGX-600
139 Engraving Machine) software. The manufacturing process required a tolerance of 0.01 mm
140 which is expected to have limited impact on the measurements.

141 Elastic guided waves are excited in correspondence of the point $E1$ by means of a ceramic
142 piezoelectric disk of 10 mm diameter bonded to the surface of the sample [43]. The plate
143 has been suspended *vertically* through wires (*as schematically reported in Fig. A1 of the*
144 *Appendix A*). *This allowed us to prevent the sample from being subjected to bending, and to*
145 *mimic the free boundary conditions implemented in the calculations. Also, we verified that*
146 *the stress induced in the unit cells by such an experimental configuration (due to the only*
147 *weight of the specimen itself) does not produce any measurable effect on the dispersion band*
148 *diagram. To achieve BG alteration, much higher levels of stress are required [25], even in the*
149 *case of extremely compliant designs [44].*

150 As the first step, a pulse made of 2 sine cycles centered at 50 kHz and modulated by a
151 Hann window is fed to the function generator. This signal has been chosen so as to generate
152 elastic waves with a much larger frequency content compared to the [45 – 53] kHz frequency
153 range of the BG highlighted in Fig. 2A. The aim is to emphasize and quantitatively evaluate
154 the screening power of the phononic region. Out-of-plane velocity is acquired through a PSV
155 400 3D scanning laser Doppler vibrometer by Polytec at the two acquisition points named
156 *O1* and *O2* (Fig. 4A), taken at the same distance from the excitation point *E1*, and chosen
157 outside and inside the phononic region of the waveguide, respectively. In both cases, 3 ms
158 long signals are recorded in order to allow multiple wave reflections to take place at both
159 the edges of the waveguide, so as to allow elastic waves to impinge on the phononic region
160 from multiple angles. After acquisition, signals are Fourier transformed and reported in
161 Fig. 4B in order to highlight the differences between the two responses in terms of frequency
162 content. The Fourier spectrum of the signal acquired outside the phononic region shows good
163 levels of transmission within the excited frequency range (30 – 90 kHz), whereas the signal
164 recorded inside the phononic region (red markers) displays a clear amplitude drop in the BG
165 region (45 – 53 kHz). This is in agreement with the dispersion diagram presented in Fig. 2A
166 and clearly confirms the possibility of the waveguide to filter waves over the [45 – 53] kHz
167 frequency range.

168 To gain further insights, full wave field reconstructions of the wave propagation phe-
169 nomena over the orange rectangular area shown in Fig. 4A are performed and compared to
170 numerical calculations. In the numerical model, elastic waves are excited by means of an
171 out-of-plane imposed displacement (of amplitude 1×10^{-6} mm). At this stage, in addition
172 to the previously described excitation, another pulse made of 21 sine cycles centered at 50
173 kHz and modulated by a Hann window is used as the excitation signal fed to the function
174 generator (and as the imposed displacement in the numerical model). In both cases, the
175 spatial scanning grid (orange rectangle in Fig. 4A) covers a 580×500 mm² of the right part
176 of the phononic plate and consists of 293×251 equally spaced grid points. A total of 10 time
177 averages were performed at each node to increase the signal to noise ratio. The knowledge of
178 the velocity time histories at all grid points allows for the reconstruction of the time-evolving
179 wavefields established in the scanning domain. Figures 4C,D show the numerical (left panels)

180 and experimental (right panels) full wavefield reconstructions of the out-of-plane velocity for
181 the Hann windowed excitation signals using 2 (Fig. 4C) and 21 (Fig. 4D) sine cycles centered
182 at 50 kHz fed in $E1$. The out-of plane velocities are normalized with respect to the respective
183 maximum amplitudes. When operating with elastic waves with a broadband energy content,
184 the laser measures transmission inside the phononic region, allowing the wavefield reconstruc-
185 tion at a comparable intensity scale with respect to points of the plate not enclosed by the
186 phononic region. However, unit cells scatter the wave field, resulting in an observable delay
187 in the wave propagation. In this case, despite the scattering, the phononic region does not
188 cause significant attenuation of the wave field. On the contrary, when observing the prop-
189 agation of an elastic wave with a narrowband energy content totally falling inside the BG,
190 strong destructive interferences due to the Bragg scattering are visible within the phononic
191 region, clearly showing that waves are reflected between the transducer and the lower edge
192 of the unit cell ring. This behavior is accompanied by an extremely low transmission due to
193 the absence of detectable wave amplitudes inside the phononic region.

194 As a final experiment, elastic guided waves are excited in correspondence of the point
195 $E2$. Among several types of excitation (larger number of cycles, other waveform shapes
196 [triangular-like, chirp-like], central frequency), the function generator has been fed with a
197 pulse made of 2 sine cycles centered at 40 kHz and modulated by a Hann window, which
198 showed to better inject energy in the system for the considered frequencies (also outside the
199 BG).

200 Out-of-plane velocity is measured along 647 equally spaced points (red dashed line re-
201 ported in Fig. 4A). Measurements are plotted as a function of the scanning position along the
202 scan line (x-axis) and time (y-axis) in Fig. 5A, where straight red lines denote the beginning
203 and the end of the periodic region. Several reflections due to the impedance mismatch are
204 clearly visible. *Signals are then 2D-Fourier transformed and reported in Fig. 5B as an in-*
205 *tensity plot of shades of grey normalized to its maximum value. Numerical dispersion curves*
206 *are superimposed to this graph for the purpose of comparison [28, 45]. Due to the type of ex-*
207 *perimental set-up, mainly out-of plane modes are expected to be excited. Therefore, in-plane*
208 *and out-of-plane polarization of the numerical modes are identified through the definition of*
209 *a polarization factor $p = \frac{\int_V (u_x)^2 dV}{\int_V [(u_x)^2 + (u_y)^2 + (u_z)^2] dV}$ for the unit cell, being V the volume of the*

210 unit cell, u_x , u_y and u_z the displacement components along x , y and z axes, respectively. As
211 a consequence, dispersion curves presented in Fig. 5B are shaded accordingly varying grad-
212 ually from 0 (blue) to 1 (green). Thus, colors close to green indicate vibration modes that
213 are dominantly polarized out-of-plane, while those close to blue are predominantly polarized
214 in-plane. A very good agreement of the two maps is found, confirming that, due to the type
215 of experimental set-up, mainly out-of plane modes are excited.

216 **3. Conclusions**

217 In this paper, we have presented a combined numerical and experimental characteriza-
218 tion procedure to validate metamaterial designs to create realistic functional wave-filtering
219 structures. We have considered an optimized design with respect to the plate thickness for
220 a phononic crystal characterized by full BGs in the kHz range, and fully demonstrated its
221 efficiency in wave propagation experiments. The design itself can be useful addition to other
222 architectures considered in the literature presenting wide BGs, with the additional advantage
223 of a simple fabrication process, e.g. by milling. More importantly, the presented experimen-
224 tal characterization procedure can serve as a general method for standardized testing and
225 evaluation of phononic crystal designs. To the best of our knowledge, this is the first work
226 to provide full experimental characterization for this type of geometry.

227 **Acknowledgments**

228 This project has received funding from the European Union’s Horizon 2020 research and
229 innovation programme under grant agreement No. 863179.

230

231 **Appendix A**

232 In this Appendix a schematic representation of how the plate was suspended during the
233 experimental phase is provided in Fig. A1.

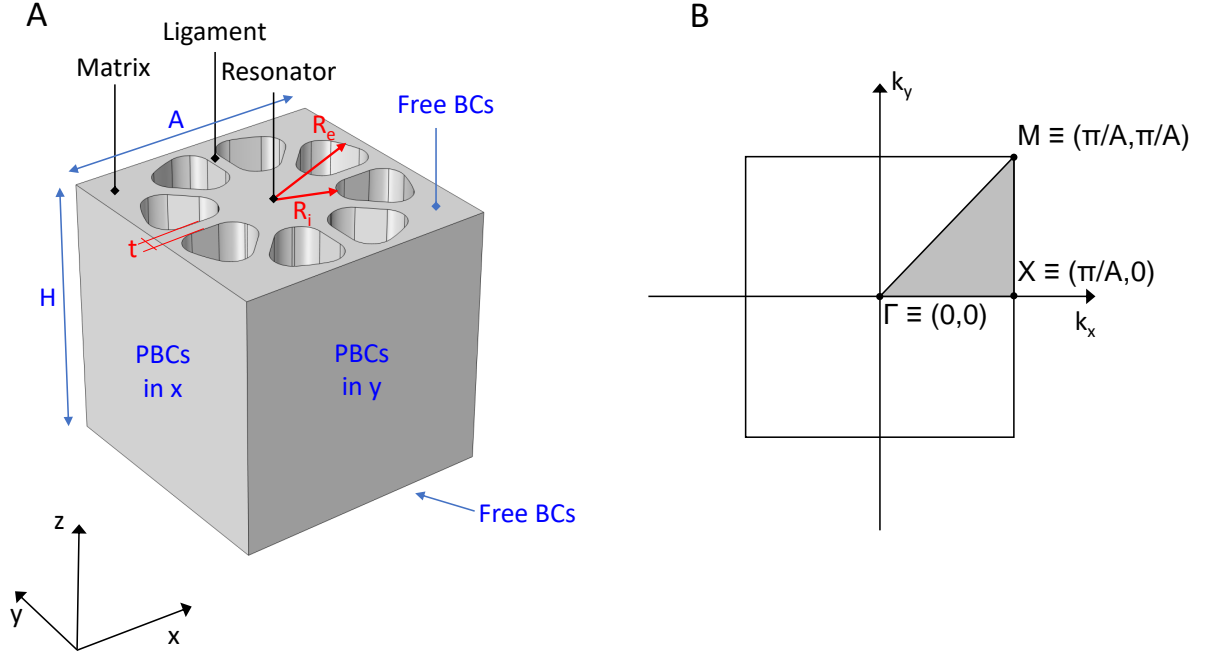


Figure 1: (A) Three-dimensional schematic representation of the unit cell investigated in this study. The structure is obtained by drilling eight cavities arranged in an octagonal pattern in a homogeneous block. The cell is thus divided into three regions, named matrix, ligaments and resonator, respectively. Geometrical parameters are the following: unit cell lattice parameter $A = H = 19$ mm, internal and external cavity radii $R_i = 4t$ and $R_e = 9t$, respectively, and ligament thickness $t = 1$ mm. (B) Schematic representation of the first irreducible Brillouin zone along the which the dispersion curves are calculated.

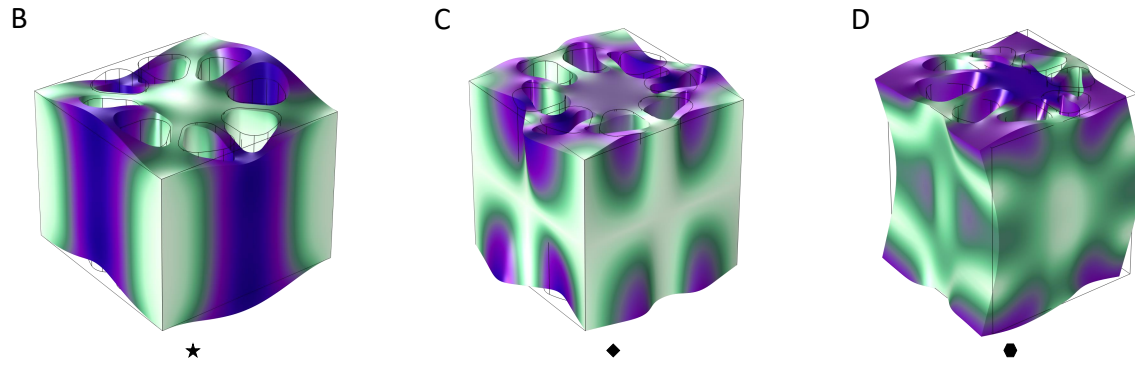
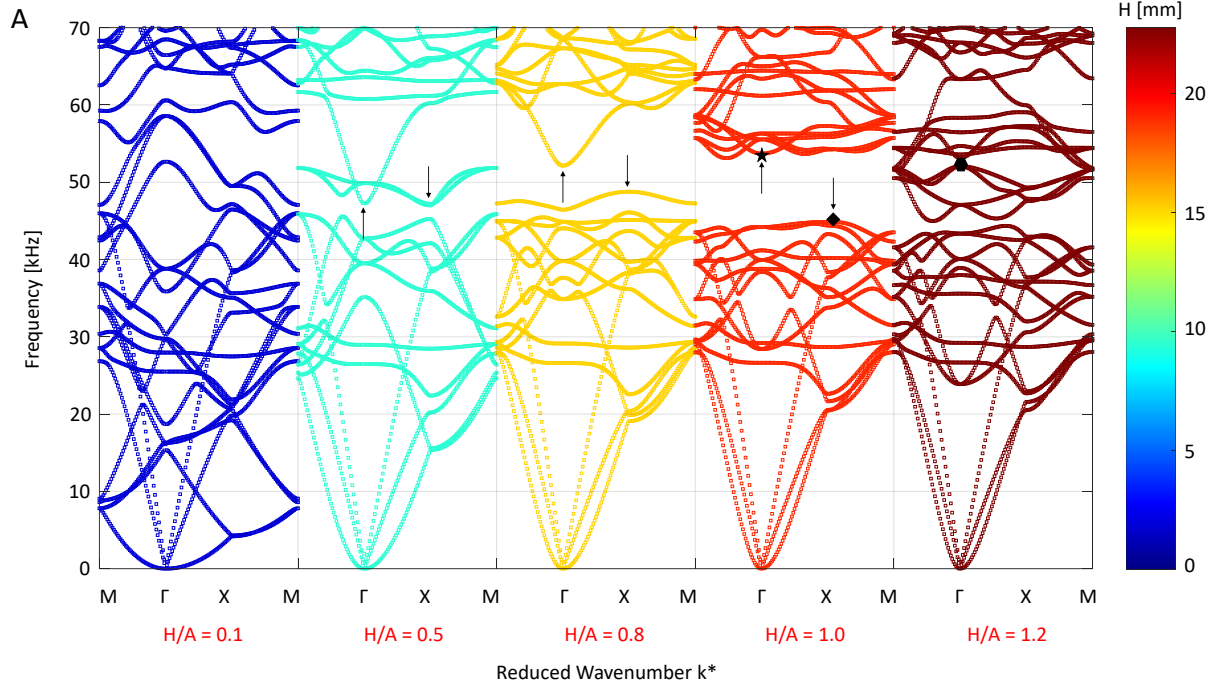


Figure 2: (A) Band diagrams along the $M - \Gamma - X - M$ Brillouin path for the unit cell reported in Fig. 1A presented as a parametric study for different height to lattice parameter ratios $H/A = [0.1, 0.5, 0.8, 1.0, 1.2]$. Curves are color coded according to the height H of the unit cell, and range from dark blue (for very thin unit cells) to dark red (for the thicker ones). The influence of the height in the opening of a BG is clearly visible. When the ratio is very small $H/A = 0.1$, no BG is present in the diagram. This is due to the extremely flexible out-of-plane properties of the unit cell, implying a large number of vibration modes in the $[0 - 70]$ kHz frequency range. When the height to lattice parameter ratio increases, fewer curves are visible in the diagram and in particular specific modes (highlighted by the black arrows) undergo a frequency shift in opposite directions. This allows to open a BG that increases its width up to a maximum width of 8 kHz achieved when $H/A = 1$. If the ratio increases above unity, additional flexural modes tend to reduce the BG width. (B-D) Deformation of the mode shapes undergoing selective frequency down(up) shift, indicated by a black star and rhombus, and located at the edges of the BG. The additional flexural mode reducing the BG width is also reported as black hexagonal marker. These modes are plotted at the Γ and X symmetry points. Color map indicates displacement magnitude.

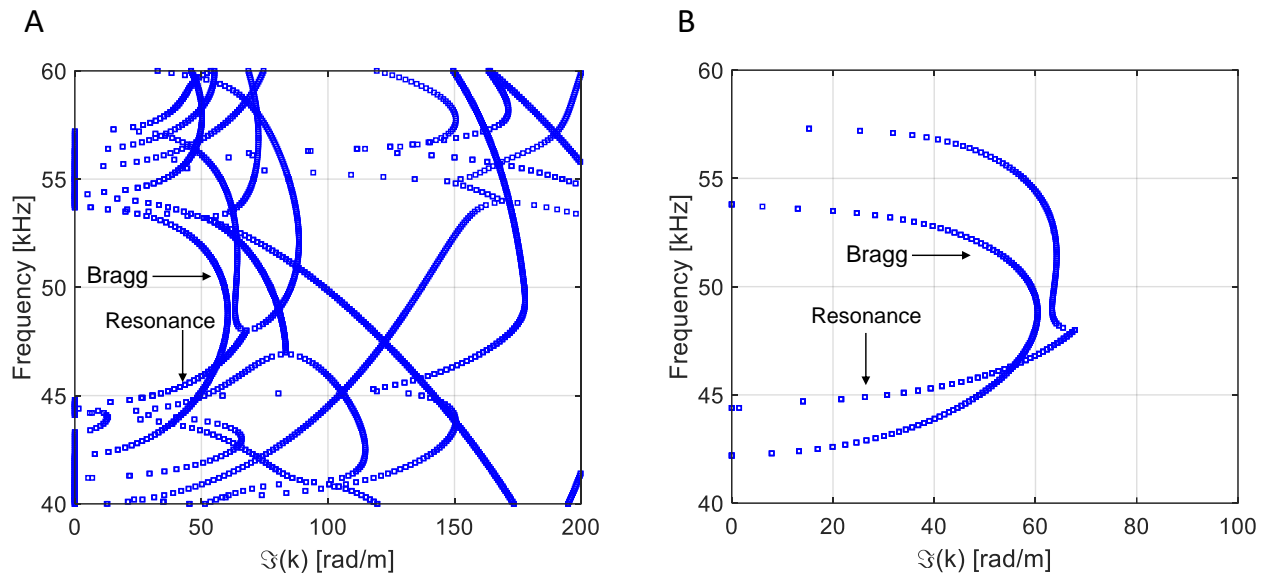


Figure 3: (A) Band diagram along the $\Gamma - X$ path for the $H/A = 1$ case reporting the frequency as a function of the imaginary part of the wavenumber, $\Im k(\omega)$. (B) Zoom in of the two isolated branches contributing to the mechanism of the BG opening. The typical parabolic and spike-like behaviors of the two curves clearly show how both Bragg and local resonance mechanisms contribute to the BG opening.

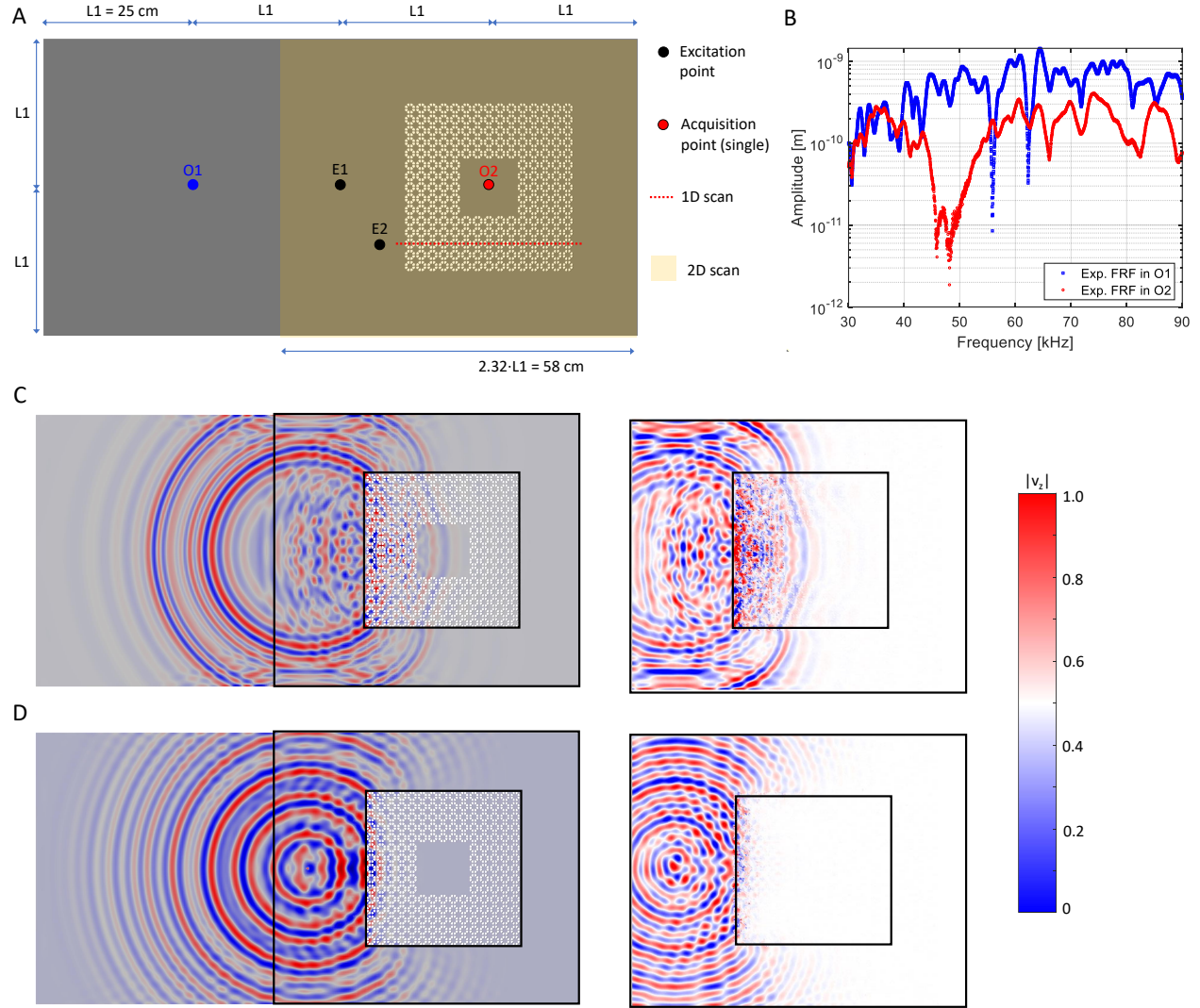


Figure 4: (A) Schematic representation of the FE model used for the three-dimensional transient dynamic computation. The specimen consists of a PMMA rectangular plate of length $4 \cdot L1 = 1000$ mm, width $2 \cdot L1 = 500$ mm and height $H = A = 19$ mm), where 200 unit cells have been drilled in the shape of a square ring. Excitation points are highlighted as black dots. Measurements are performed through Scanning Laser Doppler Vibrometry in specific points outside (blue dot named $O1$) and inside (red dot named $O2$) the phononic ring, along a 1D line scan (dotted red line), and in a 2D region scan (orange rectangle superimposed to the schematics of the plate). (B) Frequency Response Function (FRF) of the system in the $O1$ and $O2$ measurement points, both located at $L1$ from the $E1$ excitation point. A clear drop in the amplitude is visible in the frequency domain for the measurement inside the phononic region. Numerical (left panel) and experimental (right panel) full wavefield reconstructions of the out-of-plane velocity for a (C) 2 and a (D) 21 sine cycles centered at 50 kHz Hann windowed excitation signals fed in $E1$. A color map of the out-of plane velocity is reported on the right, and normalized with respect to the maximum displacement.

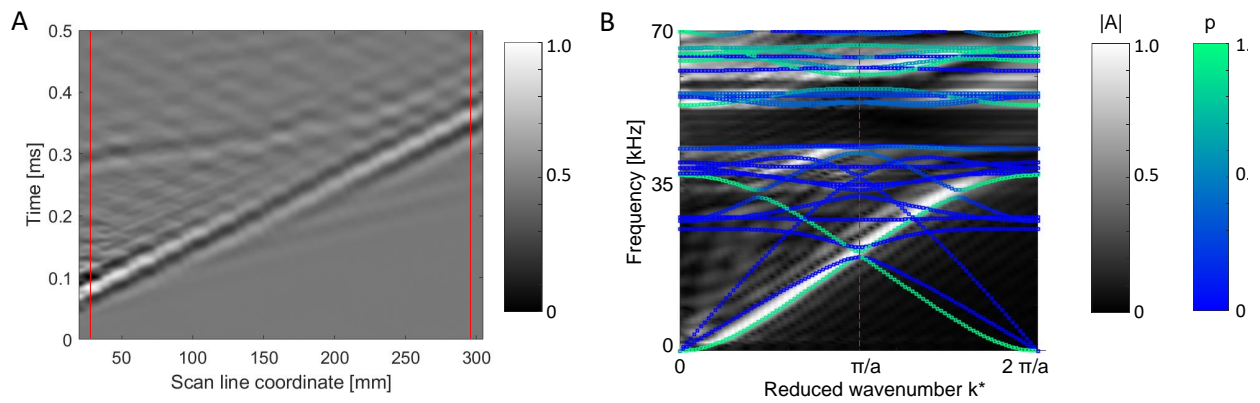


Figure 5: (A) Measured out-of-plane velocity as a function of the scanning position along the dotted red line in Fig. 4 (x-axis) and time (y-axis). Elastic waves are excited at point $E2$ using a 2 sine cycles centered at 40 kHz and Hann windowed. Red lines denote the beginning and the end of the periodic region. Several reflections due to the impedance mismatch are clearly visible. (B) Wavenumber-frequency representation of the measured signals. Numerical dispersion curves are superimposed to the experimental results. Curves are color-coded depending on their in plane / out-of-plane behavior. Due to the type of experimental set-up, mainly out-of plane modes are excited.

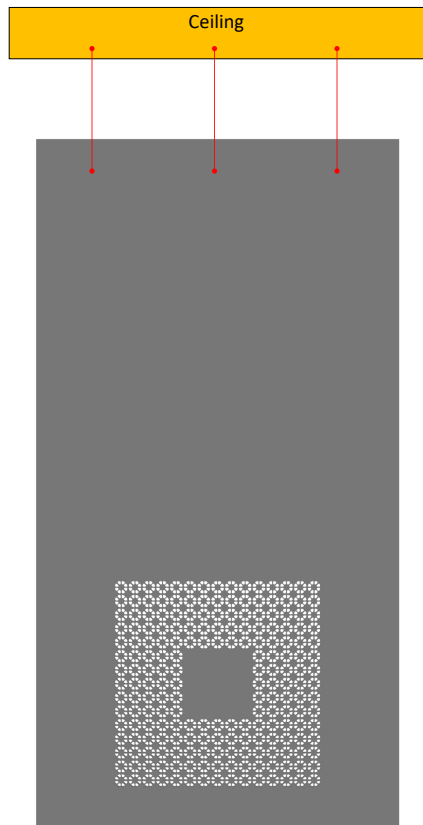


Figure A1: *Schematics of vertical hanging of the plate, allowing us to prevent the sample from being subjected to bending, and to mimic the free boundary conditions implemented in the calculations.*

234 **References**

- 235 [1] R. Martínez-Sala, J. Sancho, J. V. Sánchez, V. Gómez, J. Llinares, and F. Meseguer.
236 Sound attenuation by sculpture. *Nature*, 378(6554):241–241, 1995.
- 237 [2] P. A. Deymier. *Acoustic metamaterials and phononic crystals*, volume 173. Springer
238 Science & Business Media, 2013.
- 239 [3] Z. Liu, X. Zhang, Y. Mao, Y. Y. Zhu, Z. Yang, C. T. Chan, and P. Sheng. Locally
240 resonant sonic materials. *Science*, 289(5485):1734–1736, 2000.
- 241 [4] G. Ma and P. Sheng. Acoustic metamaterials: From local resonances to broad horizons.
242 *Science advances*, 2(2):e1501595, 2016.
- 243 [5] J. O. Vasseur, P. A. Deymier, B. Chenni, B. Djafari-Rouhani, L. Dobrzynski, and D. Pre-
244 vost. Experimental and theoretical evidence for the existence of absolute acoustic band
245 gaps in two-dimensional solid phononic crystals. *Physical Review Letters*, 86(14):3012,
246 2001.
- 247 [6] M. Miniaci, A. Marzani, N. Testoni, and L. De Marchi. Complete band gaps in a
248 polyvinyl chloride (pvc) phononic plate with cross-like holes: numerical design and ex-
249 perimental verification. *Ultrasonics*, 56:251–259, 2015.
- 250 [7] B. Morvan, A. Tinel, A.-C. Hladky-Hennion, J. O. Vasseur, and B. Dubus. Experimental
251 demonstration of the negative refraction of a transverse elastic wave in a two-dimensional
252 solid phononic crystal. *Applied Physics Letters*, 96(10):101905, 2010.
- 253 [8] J. Pierre, O. Boyko, L. Belliard, J. O. Vasseur, and B. Bonello. Negative refraction
254 of zero order flexural lamb waves through a two-dimensional phononic crystal. *Applied*
255 *Physics Letters*, 97(12):121919, 2010.
- 256 [9] V. M. García-Chocano, J. Christensen, and J. Sánchez-Dehesa. Negative refraction and
257 energy funneling by hyperbolic materials: An experimental demonstration in acoustics.
258 *Physical review letters*, 112(14):144301, 2014.

- 259 [10] D. Bigoni, S. Guenneau, A. B. Movchan, and M. Brun. Elastic metamaterials with
260 inertial locally resonant structures: Application to lensing and localization. *Physical*
261 *Review B*, 87(17):174303, 2013.
- 262 [11] A. Khelif, M. Wilm, V. Laude, S. Ballandras, and B. Djafari-Rouhani. Guided elastic
263 waves along a rod defect of a two-dimensional phononic crystal. *Physical Review E*,
264 69(6):067601, 2004.
- 265 [12] G. Bordiga, L. Cabras, D. Bigoni, and A. Piccolroaz. Free and forced wave propagation in
266 a rayleigh-beam grid: flat bands, dirac cones, and vibration localization vs isotropization.
267 *International Journal of Solids and Structures*, 161:64–81, 2019.
- 268 [13] S. H. Mousavi, A. B. Khanikaev, and Z. Wang. Topologically protected elastic waves in
269 phononic metamaterials. *Nature communications*, 6(1):1–7, 2015.
- 270 [14] R. K. Pal and M. Ruzzene. Edge waves in plates with resonators: an elastic analogue
271 of the quantum valley hall effect. *New Journal of Physics*, 19(2):025001, 2017.
- 272 [15] M. Miniaci, R. K Pal, B. Morvan, and M. Ruzzene. Experimental observation of topo-
273 logically protected helical edge modes in patterned elastic plates. *Physical Review X*,
274 8(3):031074, 2018.
- 275 [16] M. Miniaci, R. K. Pal, R. Manna, and M. Ruzzene. Valley-based splitting of topologically
276 protected helical waves in elastic plates. *Physical Review B*, 100(2):024304, 2019.
- 277 [17] C.-W. Chen, N. Lera, R. Chaunsali, D. Torrent, J. V. Alvarez, J. Yang, P. San-Jose, and
278 J. Christensen. Mechanical analogue of a majorana bound state. *Advanced Materials*,
279 31(51):1904386, 2019.
- 280 [18] G. Ma, C. Fu, G. Wang, P. Del Hougne, J. Christensen, Y. Lai, and P. Sheng. Po-
281 larization bandgaps and fluid-like elasticity in fully solid elastic metamaterials. *Nature*
282 *communications*, 7(1):1–8, 2016.
- 283 [19] M. Gei, A. B. Movchan, and D. Bigoni. Band-gap shift and defect-induced annihilation
284 in prestressed elastic structures. *Journal of Applied Physics*, 105(6):063507, 2009.

- 285 [20] R. V. Craster and S. Guenneau. *Acoustic metamaterials: Negative refraction, imaging,*
286 *lensing and cloaking*, volume 166. Springer Science & Business Media, 2012.
- 287 [21] E. Baravelli and M. Ruzzene. Internally resonating lattices for bandgap generation and
288 low-frequency vibration control. *Journal of Sound and Vibration*, 332(25):6562–6579,
289 2013.
- 290 [22] M. I Hussein, M. J. Leamy, and M. Ruzzene. Dynamics of phononic materials and
291 structures: Historical origins, recent progress, and future outlook. *Applied Mechanics*
292 *Reviews*, 66(4), 2014.
- 293 [23] S. Taniker and C. Yilmaz. Design, analysis and experimental investigation of three-
294 dimensional structures with inertial amplification induced vibration stop bands. *Inter-*
295 *national Journal of Solids and Structures*, 72:88–97, 2015.
- 296 [24] M. Mazzotti, M. Miniaci, and I. Bartoli. Band structure analysis of leaky bloch waves
297 in 2d phononic crystal plates. *Ultrasonics*, 74:140–143, 2017.
- 298 [25] M. Mazzotti, I. Bartoli, and M. Miniaci. Modeling bloch waves in prestressed phononic
299 crystal plates. *Frontiers in Materials*, 6:74, 2019.
- 300 [26] C. Sugino, M. Ruzzene, and A. Erturk. Merging mechanical and electromechanical
301 bandgaps in locally resonant metamaterials and metastructures. *Journal of the Me-*
302 *chanics and Physics of Solids*, 116:323–333, 2018.
- 303 [27] A. Bergamini, M. Miniaci, T. Delpero, D. Tallarico, B. Van Damme, G. Hannema, I.
304 Leibacher, and A. Zemp. Tacticity in chiral phononic crystals. *Nature communications*,
305 10(1):1–8, 2019.
- 306 [28] M. Miniaci, A. S. Gliozzi, B. Morvan, A. Krushynska, F. Bosia, M. Scalerandi, and N. M.
307 Pugno. Proof of concept for an ultrasensitive technique to detect and localize sources
308 of elastic nonlinearity using phononic crystals. *Physical review letters*, 118(21):214301,
309 2017.
- 310 [29] F. Ciampa, A. Mankar, and A. Marini. Phononic crystal waveguide transducers for
311 nonlinear elastic wave sensing. *Scientific reports*, 7(1):1–8, 2017.

- 312 [30] A. S. Gliozzi, M. Miniaci, A. Chiappone, A. Bergamini, B. Morin, and E. Descrovi. Tun-
313 able photo-responsive elastic metamaterials. *Nature communications*, 11(1):1–8, 2020.
- 314 [31] B. Rostami-Dogolsara, M. K. Moravvej-Farshi, and F. Nazari. Designing switchable
315 phononic crystal-based acoustic demultiplexer. *IEEE transactions on ultrasonics, ferro-*
316 *electrics, and frequency control*, 63(9):1468–1473, 2016.
- 317 [32] R. Ardito, M. Cremonesi, L. D’Alessandro, and A. Frangi. Application of optimally-
318 shaped phononic crystals to reduce anchor losses of mems resonators. In *2016 IEEE*
319 *International Ultrasonics Symposium (IUS)*, pages 1–3. IEEE, 2016.
- 320 [33] D. Misseroni, D. J. Colquitt, A. B. Movchan, N. V. Movchan, and I. . Jones. Cymatics
321 for the cloaking of flexural vibrations in a structured plate. *Scientific reports*, 6:23929,
322 2016.
- 323 [34] M. Miniaci, M. Mazzotti, M. Radziński, N. Kherraz, P. Kudela, W. Ostachowicz, B.
324 Morvan, F. Bosia, and N. M. Pugno. Experimental observation of a large low-frequency
325 band gap in a polymer waveguide. *Frontiers in Materials*, 5:8, 2018.
- 326 [35] J.-H. Sun and T.-T. Wu. Propagation of acoustic waves in phononic-crystal plates
327 and waveguides using a finite-difference time-domain method. *Physical Review B*,
328 76(10):104304, 2007.
- 329 [36] Y. Pennec, J. O. Vasseur, B. Djafari-Rouhani, L. Dobrzyński, and P. A. Deymier. Two-
330 dimensional phononic crystals: Examples and applications. *Surface Science Reports*,
331 65(8):229–291, 2010.
- 332 [37] Y. Yao, F. Wu, Z. Hou, and Z. Xin. Lamb waves in two-dimensional phononic crystal
333 plate with anisotropic inclusions. *Ultrasonics*, 51(5):602–605, 2011.
- 334 [38] M. Rupin, F. Lemoult, G. Lerosey, and P. Roux. Experimental demonstration of ordered
335 and disordered multiresonant metamaterials for lamb waves. *Physical review letters*,
336 112(23):234301, 2014.
- 337 [39] Y. Jin, B. Bonello, R. P. Moiseyenko, Y. Pennec, O. Boyko, and B. Djafari-Rouhani.
338 Pillar-type acoustic metasurface. *Physical Review B*, 96(10):104311, 2017.

- 339 [40] M. Bavencoffe, A.-C. Hladky-Hennion, B. Morvan, and J.-L. Izbicki. Attenuation of
340 lamb waves in the vicinity of a forbidden band in a phononic crystal. *IEEE transactions*
341 *on ultrasonics, ferroelectrics, and frequency control*, 56(9):1960–1967, 2009.
- 342 [41] L. De Marchi, A. Marzani, and M. Miniaci. A dispersion compensation procedure to
343 extend pulse-echo defects location to irregular waveguides. *NDT & E International*,
344 54:115–122, 2013.
- 345 [42] M. Collet, M. Ouisse, M. Ruzzene, and M. N. Ichchou. Floquet’s block decomposition
346 for the computation of dispersion of two-dimensional periodic, damped mechanical
347 systems. *International Journal of Solids and Structures*, 48(20):2837 – 2848, 2011.
- 348 [43] W. Ostachowicz, P. Kudela, M. Krawczuk, and A. Zak. *Guided Waves in Structures*
349 *for SHM: The Time - domain Spectral Element Method*. A John Wiley & Sons, Ltd.,
350 publication. Wiley, 2012.
- 351 [44] M. Miniaci, M. Mazzotti, A. Amendola, and F. Fraternali. Effect of prestress on phononic
352 band gaps induced by inertial amplification. *International Journal of Solids and Structures*,
353 2021.
- 354 [45] P. Kudela, M. Radziński, and W. Ostachowicz. Identification of cracks in thin-walled
355 structures by means of wavenumber filtering. *Mechanical Systems and Signal Processing*,
356 50:456–466, 2015.